

# Self-homodyne tomography of a twin-beam state

Giacomo M. D'Ariano,\* Michael Vasilyev, and Prem Kumar

*Department of Electrical and Computer Engineering, Northwestern University, Evanston, IL 60208, USA*

(December 2, 2024)

A self-homodyne detection scheme is proposed to perform two-mode tomography on a twin-beam state at the output of a nondegenerate optical parametric amplifier. This scheme has been devised to improve the matching between the local oscillator and the signal modes, which is the main limitation to the overall quantum efficiency in conventional homodyning. The feasibility of the measurement is analyzed on the basis of Monte-Carlo simulations, studying the effect of non-unit quantum efficiency on detection of the correlation and the total photon-number oscillations of the twin-beam state.

## I. INTRODUCTION

One of the most significant advances in modern quantum optics is the theoretical development [1] and subsequent experimental realization [2] of homodyne tomography. This measurement scheme allows one to reconstruct the density matrix of the quantum state from a set of field quadratures measured by a balanced homodyne detector. Reconstruction methods, initially based on approximate inverse Radon transform of the quadratures histograms, have been enhanced later through exact algorithms [3–6] that achieve the measurement of the matrix element by sampling a corresponding pattern function of the experimental homodyne outcomes (for a review see [7]). These algorithms have been proven to be very stable and fast enough to allow real-time data sampling. For the photon-number representation, the calculation of the pattern functions has been greatly improved by means of factorization formulas [8] and asymptotic approximations [9] for large photon numbers of the matrix indices. The direct sampling approach has been implemented experimentally to measure the photon statistics of a semiconductor laser [10], and the density matrix of a squeezed vacuum [11]. The success of optical homodyne tomography has stimulated the development of state-reconstruction procedures for atomic beams [12], the experimental determination of the vibrational state of a molecule [13], of an ensemble of helium atoms [14], and of a single ion in a Paul trap [15]. Finally, some non-tomographic state reconstruction methods have also been recently proposed [16].

While the full density matrix reconstruction requires the knowledge of the phase of the detected mode with respect to the local oscillator (LO), for the diagonal

matrix elements it is just sufficient to average over a random phase [10]. The typical nonclassical states of interest—such as squeezed states—already exhibit interesting quantum features in just the photon number distribution; this makes homodyne tomography especially attractive. Among the quantum features of interest, there are the even-odd oscillations in the photon number distribution of a squeezed vacuum [17], which were recently observed experimentally [11]. In two-mode tomography of a twin-beam state produced in parametric down-conversion, we are interested in features of the joint photon-number distribution of the signal and the idler, such as the delta-function correlation between the photon numbers of the two modes, and the even-odd oscillations of the total photon number. The sampling algorithm for the two-mode tomography is obtained by a straightforward extension of the single-mode case [18]. In the relatively new field of multimode tomography, recent advances have been made in the theoretical description [19] and the experimental measurement [20] of the photon-number correlation between two temporal modes.

From the experimental point of view, homodyne tomography of the photon-number distribution is a viable alternative to direct detection. It allows one to measure very weak photon fluxes—of the order of a fraction of a photon per measurement time—using high quantum efficiency fast *p-i-n* photodiodes, as compared to the slow and less efficient avalanche photodiodes used for direct detection. This convenience, however, comes with its own price tag. One encounters the problem of mode matching between the LO and the detected modes [21], determined by their spatial/temporal overlap, which gives a detrimental contribution to the overall quantum efficiency. As shown in Ref. [4], the detection of the quantum features is rapidly degraded by less-than-unity quantum efficiency of the homodyne detector, and the degree of degradation rapidly increases for larger photon numbers.

The problem of mode matching becomes especially severe for quantum states generated in traveling-wave or pulsed experiments, particularly those employing the optical-parametric amplifiers (OPA's). It has been shown that a LO well matched to a squeezed vacuum can be generated in the same parametric process [22]. For example, in Ref. [22] a polarizationally nondegenerate OPA was used to produce the squeezed vacuum and the matched LO in two orthogonal polarizations. However, while this approach is justified for measurements of the squeezing, it cannot be used for density-matrix reconstruction, as a tiny leakage of light from the LO polarization into the signal polarization can easily spoil the signal photon-

number distribution.

In this paper, we address the problem of generating a matched LO for the reconstruction of the density matrix of the output state of a polarization-and-frequency non-degenerate OPA. In the spirit of Ref. [22], we develop a concept of self-homodyning that allows one to create both the LO and the signal in the same OPA. In the direct detection of the output signal field, a strong mean field at the central frequency  $\omega_0$  can serve as a LO for measuring a mode that consists of two sidebands at  $\omega_0 \pm \Omega$ . As we will show in the following, the relative phase between the LO and the two-sideband mode can be varied, thus allowing homodyne tomography of the latter. In this way one can perform the tomographic reconstruction of full joint density matrix of the signal and idler twin-beam modes. In this paper, we consider the measurement of the joint photon-number distribution of these two modes and the photon-number distribution of the signal mode alone. For the latter, a thermal distribution is expected, as seen in recent self-homodyning experiments [23]. We also show that self-homodyning can be used to measure the photon statistics of the  $+45^\circ$ - and the  $-45^\circ$ -polarized linear combinations of the signal and idler modes.

From Monte-Carlo simulations we will estimate the experimental conditions that are needed to extract the joint photon-number probability distribution of the twin beams, the photon correlation between the modes, and the quantum oscillations of the total photon number. We will show how these quantities can be experimentally measured for realistic values of quantum efficiency ( $\sim 0.9$ ) of the photodiodes and for reasonable number of data points ( $\sim 10^6$ ).

In Section II we give a detailed theoretical description of the self-homodyne measurement, relating the measurement of the field quadratures to the output photocurrents in Subsection II A, and evaluating the joint probability distribution of the photocurrents in Subsection II B, in a form suitable for Monte-Carlo simulations, also taking into account the effect of non-unit quantum efficiency. In Section III we briefly review the exact reconstruction algorithm for quantum tomography, for one mode only in Subsection III A, and then with extension to any number of modes in Subsection III B. In Subsection III C we analyze how the two-mode tomography is achieved through self-homodyne detection. In Subsection III D we introduce the concepts of the measurement of the “dressed” state, often adopted in experiments,—as opposed to the “bare” state, usually assumed by the theorists. In Section IV we present some selected Monte-Carlo simulations, also for non-unit quantum efficiency, for both the bare and the dressed states. We will focus attention on the joint photon-number probability, on the correlation between the photon numbers of the two modes, and finally on the total photon-number probability, which exhibits oscillations typical of the twin-beam state. Section V concludes the paper with a discussion of the results in view of the feasibility of the real experiment. The Appendix covers the details of derivation of the joint pho-

tocurrent distribution used in Subsection II B.

## II. THEORETICAL DESCRIPTION OF THE SELF-HOMODYNE MEASUREMENT

### A. The detector

The scheme of a self-homodyne detector is depicted in Fig. 1, along with the relevant modes of the electromagnetic field involved in the measurement. A nondegenerate optical parametric amplifier (NOPA) is injected with an input field having a strong coherent component at frequency  $\omega_0$  with amplitudes  $\alpha_\uparrow$  and  $\alpha_\leftrightarrow$  depending on the polarization,  $\uparrow$  denoting the vertical and  $\leftrightarrow$  the horizontal polarization, respectively. The amplifier is pumped at the second harmonic  $\omega_p = 2\omega_0$  with amplitude  $\alpha_p \gg \alpha_\uparrow, \alpha_\leftrightarrow$ , such that the pump can be considered as classical and undepleted during the amplification process. At the output of the amplifier two photodetectors separately measure the intensities of a couple of orthogonally-polarized components of the field  $\hat{\mathcal{E}}_\uparrow$  and  $\hat{\mathcal{E}}_\leftrightarrow$ . At the output of the photodetectors, a narrow band of the photocurrent is selected, centered around frequency  $\Omega \ll \omega_0$  (typically  $\omega_0$  is optical/infrared, whereas  $\Omega$  is a radio frequency). In the narrowband approximation and for radiation absorbed in a thin detector layer, the filtered output photocurrents are given by the (complex) operators

$$\begin{aligned} \hat{I}_\pi(\Omega) &\propto \int_{-\infty}^{+\infty} dt e^{i\Omega t} : |\hat{\mathcal{E}}_\pi(t)|^2 : \\ &= \int_{-\infty}^{+\infty} d\omega \hat{\mathcal{E}}_\pi^-(\omega + \Omega) \hat{\mathcal{E}}_\pi^+(\omega), \quad \pi = \{\uparrow, \leftrightarrow\}, \end{aligned} \quad (1)$$

where  $::$  denote the customary normal ordering with the (output) field annihilation-operator components  $\hat{\mathcal{E}}_\pi^+$  on the right and the creation operators  $\hat{\mathcal{E}}_\pi^-$  on the left, and the subindex  $\pi$  runs on the two independent polarizations  $\uparrow$  and  $\leftrightarrow$ . In terms of the annihilation and creation operators  $\hat{b}$  and  $\hat{b}^\dagger$  of the relevant output modes one has

$$\hat{I}_\pi(\Omega) = \hat{b}_{0\pi}^\dagger \hat{b}_{-\pi} + \hat{b}_{+\pi}^\dagger \hat{b}_{0\pi}, \quad (2)$$

where the subindex 0 refers to the central mode at frequency  $\omega_0$ , and  $\pm$  refer to the sidebands at frequencies  $\omega_0 \pm \Omega$ , respectively. The input-output Heisenberg evolutions of the relevant field modes across the NOPA are given by

$$\begin{aligned} \hat{b}_{0\uparrow} &= \mu \hat{a}_{0\uparrow} + \nu \hat{a}_{0\leftrightarrow}^\dagger, & \hat{b}_{0\leftrightarrow} &= \mu \hat{a}_{0\leftrightarrow} + \nu \hat{a}_{0\uparrow}^\dagger, \\ \hat{b}_{+\uparrow} &= \mu \hat{a}_{+\uparrow} + \nu \hat{a}_{-\leftrightarrow}^\dagger, & \hat{b}_{+\leftrightarrow} &= \mu \hat{a}_{+\leftrightarrow} + \nu \hat{a}_{-\uparrow}^\dagger, \\ \hat{b}_{-\uparrow} &= \mu \hat{a}_{-\uparrow} + \nu \hat{a}_{+\leftrightarrow}^\dagger, & \hat{b}_{-\leftrightarrow} &= \mu \hat{a}_{-\leftrightarrow} + \nu \hat{a}_{+\uparrow}^\dagger, \end{aligned} \quad (3)$$

where  $a$  and  $a^\dagger$  denote the annihilation and creation operators for the input modes,  $\mu = \cosh r$ ,  $\nu = e^{i\theta_p} \sinh r$ ,

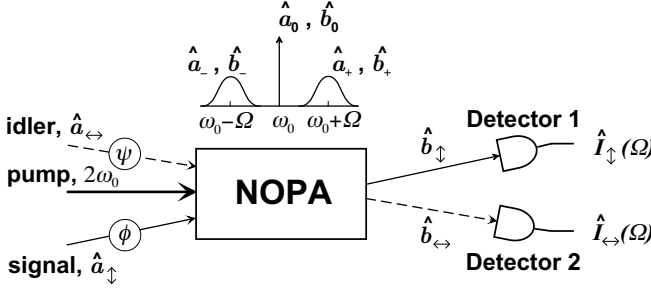


FIG. 1. Scheme of a self-homodyne detector along with the relevant modes of the electromagnetic field involved in the measurement. The nondegenerate optical parametric amplifier (NOPA) is seeded with input fields having strong coherent components at frequency  $\omega_0$ , and is pumped at the second harmonic  $\omega_p = 2\omega_0$ . At the output of the amplifier the intensities of the two different polarizations are separately measured by photodetectors, and a narrow band of the output photocurrents is selected, centered around frequency  $\Omega \ll \omega_0$ .

$r \propto L\chi^{(2)}|\alpha_p|$  ( $L$  is the amplifier length,  $\chi^{(2)}$  is the effective second-order susceptibility). In the following we put  $\theta_p = 0$ , namely we set the pump phase as the reference phase for all modes. We assume the mode  $\hat{a}_{0\uparrow}$  to be in a highly excited coherent state with amplitude  $\alpha_{\uparrow}$ . For the purpose of measurement of the joint photon-number distribution, the mode  $\hat{a}_{0\leftrightarrow}$  will also be assumed in a highly excited coherent state with amplitude  $\alpha_{\leftrightarrow}$ . In the case where we are interested in measuring the photon-number distribution of one beam only, the photocurrent produced by the ' $\leftrightarrow$ '-polarized beam can be ignored or the mode  $\hat{a}_{0\leftrightarrow}$  can be assumed to be in the vacuum state. In the process of direct detection, the highly-excited central modes  $\hat{a}_{0\uparrow,\leftrightarrow}$  beat with the  $\omega_0 \pm \Omega$  sideband modes, thus playing the role of the LO of homodyne and heterodyne detectors. This converts the direct detectors into self-homodyne detectors whose experimental outcomes are the measured values of the following rescaled output photocurrents in the limit of strong LO's:

$$\begin{aligned}\hat{I}_{\uparrow}(\Omega) &= \lim_{|\alpha| \rightarrow \infty} \frac{\text{Tr}_{\text{LO}}[\hat{I}_{\uparrow}(\Omega)\hat{\rho}_{\text{LO}}]}{\sqrt{2}\eta_{\uparrow}|\mu\alpha_{\uparrow} + \nu\alpha_{\uparrow}^*|}, \\ \hat{I}_{\leftrightarrow}(\Omega) &= \lim_{|\alpha| \rightarrow \infty} \frac{\text{Tr}_{\text{LO}}[\hat{I}_{\leftrightarrow}(\Omega)\hat{\rho}_{\text{LO}}]}{\sqrt{2}\eta_{\leftrightarrow}|\mu\alpha_{\leftrightarrow} + \nu\alpha_{\uparrow}^*|},\end{aligned}\quad (4)$$

where  $\eta_{\uparrow}$  and  $\eta_{\leftrightarrow}$  denote the quantum efficiencies of the two photodetectors,  $\alpha^*$  denotes the complex conjugate of  $\alpha$ ,  $\hat{\rho}_{\text{LO}}$  represents the density operator of the LO state, and  $\text{Tr}_{\text{LO}}$  denotes the partial trace over the LO modes. In Eq. (4)  $\hat{I}_{\pi}(\Omega)$  is modified from that in Eq. (2) because of the non-unity quantum efficiencies of the two photodetectors. It is given by

$$\hat{I}_{\pi}(\Omega) = \hat{b}'_{0\pi}^{\dagger}\hat{b}'_{-\pi} + \hat{b}'_{+\pi}^{\dagger}\hat{b}'_{0\pi}, \quad (5)$$

where  $\hat{b}'_{\gamma\pi} = \sqrt{\eta_{\pi}}\hat{b}_{\gamma\pi} + \sqrt{1-\eta_{\pi}}\hat{v}_{\gamma\pi}$ . Here  $\hat{v}_{\gamma\pi}$  for  $\gamma \in \{0, +, -\}$  and  $\pi \in \{\uparrow, \leftrightarrow\}$  are independent vacuum-state

operators accounting for the loss at the three frequency components of each polarization mode. For the sake of simplicity, we will assume  $\eta_{\uparrow} = \eta_{\leftrightarrow} = 1$  for the rest of this Subsection. We will take into account the effect of non-unity quantum efficiency on the photocurrent probability distribution in Subsection II B. Thus, using Eqs. (3) and quantum efficiency equal to unity, one obtains [24]

$$\begin{aligned}\hat{I}_{\uparrow}(\Omega) &= \frac{1}{\sqrt{2}}(e^{-i\phi}\hat{b}_{-\uparrow} + e^{i\phi}\hat{b}_{+\uparrow}^{\dagger}), \\ \hat{I}_{\leftrightarrow}(\Omega) &= \frac{1}{\sqrt{2}}(e^{-i\psi}\hat{b}_{-\leftrightarrow} + e^{i\psi}\hat{b}_{+\leftrightarrow}^{\dagger}),\end{aligned}\quad (6)$$

where  $\phi = \arg(\alpha_{\uparrow} + \tau\alpha_{\leftrightarrow}^*)$  is the phase of the mode  $\hat{b}_{0\uparrow}$  relative to that of the pump with  $\tau = \tanh r$ , and analogously  $\psi = \arg(\alpha_{\leftrightarrow} + \tau\alpha_{\uparrow}^*)$ . Taking the real part of the photocurrents at given radio-frequency phases  $\xi$  and  $\chi$  one has

$$\begin{aligned}\text{Re}[\hat{I}_{\uparrow}(\Omega)e^{i\xi}] &= \hat{X}_{\phi}(\hat{B}_{\uparrow}^{(\xi)}), \\ \text{Re}[\hat{I}_{\leftrightarrow}(\Omega)e^{i\chi}] &= \hat{X}_{\psi}(\hat{B}_{\leftrightarrow}^{(\chi)}),\end{aligned}\quad (7)$$

where the operator  $\hat{X}_{\phi}(\hat{c})$  denotes the quadrature at phase  $\phi$  of the mode with annihilation operator  $\hat{c}$ , namely,

$$\hat{X}_{\phi}(\hat{c}) = \frac{1}{2}(e^{-i\phi}\hat{c} + e^{i\phi}\hat{c}^{\dagger}), \quad (8)$$

and the operator  $\hat{B}_{\pi}^{(\lambda)}$  is the annihilator of the polarized output mode

$$\hat{B}_{\pi}^{(\lambda)} = \frac{1}{\sqrt{2}}(e^{i\lambda}\hat{b}_{-\pi} + e^{-i\lambda}\hat{b}_{+\pi}). \quad (9)$$

It is easy to check that the output modes (9) have corresponding input modes given by

$$\hat{A}_{\pi}^{(\lambda)} = \frac{1}{\sqrt{2}}(e^{i\lambda}\hat{a}_{-\pi} + e^{-i\lambda}\hat{a}_{+\pi}), \quad (10)$$

and they are related by the Heisenberg evolutions

$$\begin{aligned}\hat{B}_{\uparrow}^{(\lambda)} &= \mu\hat{A}_{\uparrow}^{(\lambda)} + \nu\hat{A}_{\leftrightarrow}^{(\lambda)\dagger}, \\ \hat{B}_{\leftrightarrow}^{(\lambda)} &= \mu\hat{A}_{\leftrightarrow}^{(\lambda)} + \nu\hat{A}_{\uparrow}^{(\lambda)\dagger}.\end{aligned}\quad (11)$$

By scanning the relative phase  $\phi$  between  $\hat{b}_{0\uparrow}$  and the pump mode, one can measure any quadrature  $\hat{X}_{\phi}(\hat{B}_{\uparrow}^{(\xi)})$  of the output field. If the input sideband modes  $\hat{a}_{\pm}$  are in a state with a completely random phase, such as the vacuum, then the only phase reference in the output modes  $\hat{b}_{\pm}$  is the pump phase  $\theta_p = 0$ . In that case, the phase  $\phi$  can be easily changed by delaying all the input fields with respect to the pump field, with no need to change the phase of  $\hat{a}_{0\uparrow}$  separately from the other input modes.

From Eq. (9) one can recognize that there are actually four output modes that commute with each other; hence,

their quadratures could be jointly measured by the self-homodyne detectors. They are  $\hat{B}_{\uparrow}^{(\xi)}$ ,  $\hat{B}_{\uparrow}^{(\xi+\pi/2)}$ ,  $\hat{B}_{\leftrightarrow}^{(\chi)}$ , and  $\hat{B}_{\leftrightarrow}^{(\chi+\pi/2)}$ , corresponding to the “cosine” and “sine” components of the two photocurrents in Eqs. (6) at phases  $\xi$  and  $\chi$  respectively. The modes  $\hat{B}_{\uparrow}^{(\lambda)}$  and  $\hat{B}_{\leftrightarrow}^{(\lambda)}$  are correlated due to the parametric interaction in Eq. (11). This interaction, however, does not couple the modes  $\hat{B}_{\uparrow}^{(\lambda)}$  and  $\hat{B}_{\leftrightarrow}^{(\lambda+\pi/2)}$ .

## B. Photocurrent probability distribution

Since we are interested in using self-homodyne detection to measure the quadratures of two correlated modes  $\hat{B}_{\uparrow}^{(\lambda)}$  and  $\hat{B}_{\leftrightarrow}^{(\lambda)}$ , the radio-frequency phase  $\lambda$  can always be set to zero by shifting the time origin. Then, the quadratures  $\hat{X}_{\phi}(\hat{B}_{\uparrow}^{(0)})$  and  $\hat{X}_{\psi}(\hat{B}_{\leftrightarrow}^{(0)})$  are jointly measured. In the following we will use the shorthand notation  $\hat{B}_{\pi} \equiv \hat{B}_{\pi}^{(0)}$  and  $\hat{X}_{\phi}^{\pi} \equiv \hat{X}_{\phi}(\hat{B}_{\pi}^{(0)})$ , and analogously for the input modes  $\hat{A}_{\pi} \equiv \hat{A}_{\pi}^{(0)}$ . For perfect detectors, the joint probability distribution of the “cosine” photocurrents with  $\xi = \chi$  in Eqs. (7) coincides with the joint probability distribution of the two quadratures  $\hat{X}_{\phi}^{\uparrow}$  and  $\hat{X}_{\phi}^{\leftrightarrow}$ , namely,

$$p(x, x'; \phi, \psi) = \langle x, x'; \phi, \psi | \hat{R} | x, x'; \phi, \psi \rangle, \quad (12)$$

where  $|x, x'; \phi, \psi\rangle \doteq |x\rangle_{\phi} \otimes |x'\rangle_{\psi}$  represents the simultaneous eigenvector of the two quadratures  $\hat{X}_{\phi}^{\uparrow}$  and  $\hat{X}_{\phi}^{\leftrightarrow}$  with eigenvalues  $x$  and  $x'$  in the Fock space  $\mathcal{H}_{\uparrow} \otimes \mathcal{H}_{\leftrightarrow}$  of the two modes  $\hat{B}_{\uparrow}$  and  $\hat{B}_{\leftrightarrow}$ , respectively; and  $\hat{R}$  denotes their joint density operator. For detectors with non-unit quantum efficiencies  $\eta_{\uparrow}$  and  $\eta_{\leftrightarrow}$ , the joint probability distribution  $p_{\eta_{\uparrow}\eta_{\leftrightarrow}}(x, x'; \phi, \psi)$  of the photocurrents is the convolution [24] of the ideal probability in Eq. (12) with Gaussians for each mode of variances

$$\Delta_{\eta_{\pi}}^2 = \frac{1 - \eta_{\pi}}{4\eta_{\pi}}. \quad (13)$$

In this way, the resulting output probability distribution can be written in the form

$$p_{\eta_{\uparrow}\eta_{\leftrightarrow}}(x, x'; \phi, \psi) = \frac{1}{2\pi\Delta_{\eta_{\uparrow}}\Delta_{\eta_{\leftrightarrow}}} \times \text{Tr} \left\{ \hat{R} \exp \left[ -\frac{(x - \hat{X}_{\phi}^{\uparrow})^2}{2\Delta_{\eta_{\uparrow}}^2} - \frac{(x' - \hat{X}_{\psi}^{\leftrightarrow})^2}{2\Delta_{\eta_{\leftrightarrow}}^2} \right] \right\}. \quad (14)$$

For simplicity, in the following we will assume equal quantum efficiencies  $\eta_{\uparrow} = \eta_{\leftrightarrow} \equiv \eta$  for both detectors. Notice that in the limit of unit quantum efficiency,  $\eta \rightarrow 1$ , one has  $\Delta_{\eta} \rightarrow 0$ , and the ideal probability in (12) is recovered.

We are now interested in the simplest case of measurement, that with  $\omega_0 \pm \Omega$  sidebands in the vacuum state

at the input of the NOPA (i.e., parametric fluorescence). In the Schrödinger picture, Eqs. (11) correspond to the following state generated at the output of the NOPA:

$$|\Psi\rangle = (1 - \tau^2)^{1/2} \sum_{n=0}^{\infty} \tau^n |n, n\rangle, \quad (15)$$

where  $\tau = \tanh r$ , and the two-mode Fock state  $|n, m\rangle$  pertaining to  $\hat{B}_{\uparrow}$  and  $\hat{B}_{\leftrightarrow}$  is given by

$$|n, m\rangle \doteq \frac{\left(\hat{B}_{\uparrow}^{\dagger}\right)^n \left(\hat{B}_{\leftrightarrow}^{\dagger}\right)^m}{\sqrt{n!m!}} |0, 0\rangle, \quad (16)$$

where  $|0, 0\rangle$  denotes the vacuum for both the  $\hat{B}_{\pi}$  modes. For the state (15) the photon-number probability is given by

$$p(n, m) \doteq |\langle n, m | \Psi \rangle|^2 = \delta_{nm} (1 - \tau^2) \tau^{2n} = \frac{\delta_{nm}}{\bar{n} + 1} \left( \frac{\bar{n}}{\bar{n} + 1} \right)^n, \quad (17)$$

where

$$\bar{n} = \frac{\tau^2}{1 - \tau^2} = \nu^2 = \sinh^2 r \quad (18)$$

is the average number of photons in each mode at the NOPA output due to parametric fluorescence. The main feature of the distribution (17) is the perfect correlation of the photon numbers in the signal and idler modes. The two-mode photon-number probability  $p(n, m)$  of Eq. (17) is shown in Fig. 2(left).

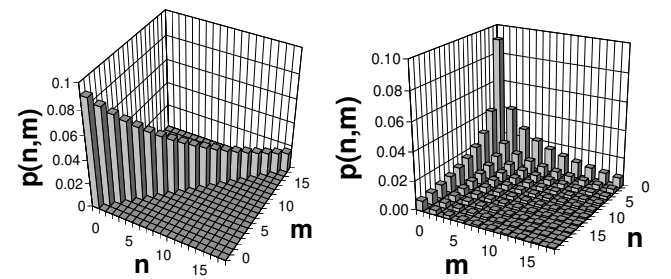


FIG. 2. Theoretical two-mode photon-number probability  $p(n, m)$  of parametric fluorescence in the signal and idler (twin-beam) modes (left), and in the  $\pm 45^\circ$ -polarized modes (right), given by Eqs. (17) and (26), correspondingly. The mean number of photons in each mode  $\bar{n} = 10$ .

The joint probability distribution of the output photocurrents is derived in the Appendix, and is given by

$$p_{\eta}(x, x'; \phi, \psi) \doteq \frac{1}{2\pi\Delta_{\eta}^2} \times \left\langle \Psi \left| \exp \left\{ -\frac{1}{2\Delta_{\eta}^2} [(x - \hat{X}_{\phi}^{\uparrow})^2 + (x' - \hat{X}_{\psi}^{\leftrightarrow})^2] \right\} \right| \Psi \right\rangle \quad (19)$$

$$= \frac{2}{\pi \sqrt{(d_\kappa^2 + 4\Delta_\eta^2)(d_{-\kappa}^2 + 4\Delta_\eta^2)}} \\ \times \exp \left[ -\frac{(x+x')^2}{d_\kappa^2 + 4\Delta_\eta^2} - \frac{(x-x')^2}{d_{-\kappa}^2 + 4\Delta_\eta^2} \right], \quad (20)$$

which can also be cast in the equivalent form

$$p(x, x'; \phi, \psi) = \frac{a_\kappa b_\kappa}{\pi} \exp \left[ -a_\kappa^2(x - c_\kappa x')^2 - b_\kappa^2 x'^2 \right], \quad (21)$$

where

$$\begin{aligned} \kappa &= e^{-i(\phi+\psi)} \tanh r, \\ d_\kappa^2 &= \frac{|1+\kappa|^2}{1-|\kappa|^2}, \\ a_\kappa^2 &= \frac{d_\kappa^2 + d_{-\kappa}^2 + 8\Delta_\eta^2}{(d_\kappa^2 + 4\Delta_\eta^2)(d_{-\kappa}^2 + 4\Delta_\eta^2)}, \\ c_\kappa &= \frac{d_\kappa^2 - d_{-\kappa}^2}{d_{-\kappa}^2 + d_\kappa^2 + 8\Delta_\eta^2}, \\ b_\kappa^2 &= a_\kappa^2(1 - c_\kappa^2). \end{aligned}$$

In the case that we measure only a single output photocurrent, say  $\hat{I}_\uparrow(\Omega)$ —namely, we ignore the measured value of the other photocurrent  $\hat{I}_\leftrightarrow(\Omega)$ —the self-homodyne detector is equivalent to a conventional homodyne detector, which measures only the quadrature  $\hat{X}_\phi^\uparrow$  of mode  $\hat{B}_\uparrow$ . The output probability distribution is given by

$$p_\eta(x; \phi) \doteq \frac{1}{\sqrt{2\pi\Delta_\eta^2}} \text{Tr} \left\{ \hat{\rho} \exp \left[ -\frac{(x - \hat{X}_\phi^\uparrow)^2}{2\Delta_\eta^2} \right] \right\}, \quad (22)$$

where the reduced density operator of the mode  $\hat{B}_\uparrow$  is

$$\hat{\rho} = \text{Tr}_\leftrightarrow [|\Psi\rangle\langle\Psi|] = \frac{1}{\bar{n}+1} \left( \frac{\bar{n}}{\bar{n}+1} \right)^{\hat{B}_\uparrow^\dagger \hat{B}_\uparrow} \quad (23)$$

with  $\text{Tr}_\leftrightarrow$  denoting the partial trace over the Hilbert space of the undetected mode  $\hat{B}_\leftrightarrow$ . The reduced density operator of the mode  $\hat{B}_\uparrow$  in Eq. (23) is that of a thermal state with the photon-number probability

$$p(n) = \frac{1}{\bar{n}+1} \left( \frac{\bar{n}}{\bar{n}+1} \right)^n, \quad (24)$$

where the average photon number  $\bar{n}$  is given by Eq. (18). The probability distribution of the output photocurrent, Eq. (22), is a Gaussian with variance  $\Delta^2 = \frac{1}{2}(\bar{n} + \frac{1}{2}) + \Delta_\eta^2$ , centered at zero. This result of self-homodyning of only the signal mode has been recently demonstrated experimentally [23].

Let us note that, while our analysis is aimed at the measurement of the joint signal-idler photon distribution, a similar self-homodyning approach can also be

implemented to measure the joint distribution of  $\pm 45^\circ$ -polarized OPA outputs. In that case, a quadrature of the annihilation operator

$$\hat{B}_\pi = \mu \hat{A}_\pi + \nu \hat{A}_\pi^\dagger \quad (25)$$

is detected at a phase  $\arg(\alpha_\pi + \tau\alpha_\pi^*)$ , where the subindex  $\pi$  runs on the two independent  $\pm 45^\circ$  polarizations, namely  $\nearrow$  and  $\nwarrow$ , and  $\alpha_\pi$  is the coherent-state amplitude of the corresponding central-frequency component of the input. Since the interaction (25) does not couple the  $+45^\circ$  and  $-45^\circ$  modes with each other, the polarization non-degenerate OPA is equivalent to two degenerate OPA's. Two-mode joint photon-number distribution is just a product of the marginal distributions for each mode, and in the case of vacuum-state input sidebands is given by [17]

$$\begin{aligned} p(n, m) &= 0 \quad \text{for } n = 2k+1 \text{ or } m = 2l+1, \\ p(n, m) &= \frac{(2k-1)!! (2l-1)!!}{2^{k+l} k! l!} \frac{1}{\bar{n}+1} \left( \frac{\bar{n}}{\bar{n}+1} \right)^{k+l} \\ &\quad \text{for } n = 2k, m = 2l, \end{aligned} \quad (26)$$

where the mean photon number  $\bar{n}$  in each mode is given by Eq. (18). The probability distribution (26) is shown in Fig. 2(right), next to the signal-idler joint photon-number distribution of Eq. (17). While the  $\pm 45^\circ$  modes exhibit independent photon-number oscillations in Fig. 2(right), the signal and idler correlations in Fig. 2(left) result in oscillations of the total photon number.

### III. QUANTUM HOMODYNE TOMOGRAPHY

In this section we briefly review the method for reconstructing the quantum state that was introduced in Refs. [3,4] for one field mode. Then we show how it can be straightforwardly extended to any number of modes—in particular, to the case of two modes involved in the self-homodyne detection of the OPA output—and we will obtain an algorithm similar to those in Refs. [18]. Finally, we introduce the measurement of the “dressed” state, often performed in experiments, as opposed to the “bare” state, typically assumed by the theorists.

#### A. Single mode detection

The method for reconstructing the matrix elements of the density operator is based on the following resolution of the identity on the Hilbert-Schmidt space

$$\hat{\rho} = \int \frac{d^2 w}{\pi} \text{Tr}[\hat{\rho} \hat{D}(w)] \hat{D}^\dagger(w), \quad (27)$$

where the integral is extended to the complex plane  $\mathbf{C}$  for  $w$ , and  $\hat{D}(w) = \exp(-w^* \hat{a} + w \hat{a}^\dagger)$  denotes the displacement operator for the field mode of interest with annihilation operator  $\hat{a}$ . Equation (27) simply follows from the orthogonality relation for displacement operators

$$\text{Tr}[\hat{D}(w)\hat{D}^\dagger(v)] = \delta_2(w - v), \quad (28)$$

where  $\delta_2(w)$  denotes the Dirac delta-function on the complex plane. By changing to polar variables  $w = (i/2)ke^{i\phi}$ , Eq. (27) becomes

$$\hat{\varrho} = \int_0^\pi \frac{d\phi}{\pi} \int_{-\infty}^{+\infty} \frac{dk |k|}{4} \text{Tr}(\hat{\varrho} e^{ik\hat{X}_\phi}) e^{-ik\hat{X}_\phi}, \quad (29)$$

where  $\hat{X}_\phi = \frac{1}{2}(\hat{a}^\dagger e^{i\phi} + \hat{a} e^{-i\phi})$  denotes the quadrature operator for the field mode  $\hat{a}$ . Then we evaluate the trace using the eigenvectors  $\{|x\rangle_\phi\}$  of  $\hat{X}_\phi$ , and multiply and divide the function inside the integral by  $\exp[(1 - \eta)k^2/(8\eta)]$  in the following fashion:

$$\begin{aligned} \hat{\varrho} &= \int_0^\pi \frac{d\phi}{\pi} \int_{-\infty}^{+\infty} \frac{dk |k|}{4} e^{-\frac{1-\eta}{8\eta}k^2} \\ &\times \int_{-\infty}^{+\infty} dx p(x, \phi) e^{ikx} e^{\frac{1-\eta}{8\eta}k^2} e^{-ik\hat{X}_\phi}, \end{aligned} \quad (30)$$

where  $p(x, \phi) = \langle x | \hat{\varrho} | x \rangle_\phi$  is the ideal homodyne probability. Using the convolution theorem we obtain

$$\hat{\varrho} = \int_0^\pi \frac{d\phi}{\pi} \int_{-\infty}^{+\infty} dx p_\eta(x; \phi) \hat{K}_\eta(x - \hat{X}_\phi), \quad (31)$$

where  $p_\eta(x; \phi)$  is the homodyne probability distribution for non-unit quantum efficiency  $\eta$ , which is the convolution of  $p(x, \phi)$  with a Gaussian of variance  $\Delta_\eta^2$  given in Eq. (13). The kernel  $\hat{K}_\eta(x - \hat{X}_\phi)$  in Eq. (31) is formally given by

$$\begin{aligned} \hat{K}_\eta(x - \hat{X}_\phi) &= \\ \frac{1}{2} \text{Re} \int_0^{+\infty} dk k \exp \left[ \frac{1-\eta}{8\eta} k^2 + ik(x - \hat{X}_\phi) \right], \end{aligned} \quad (32)$$

where convergence of the integral in Eq. (32) for the operator  $\hat{K}_\eta(x - \hat{X}_\phi)$  is intended in the weak sense of convergence of the matrix elements  $\langle v | \hat{K}_\eta(x - \hat{X}_\phi) | v' \rangle$  between the Hilbert-space vectors  $|v\rangle$  and  $|v'\rangle$ , which are evaluated before integration. From Eq. (31) it follows that the matrix element  $\langle v | \hat{\varrho} | v' \rangle$  can be experimentally obtained by averaging the function  $\langle v | \hat{K}_\eta(x - \hat{X}_\phi) | v' \rangle$  over the quadrature outcomes  $x$  that are homodyne detected at random phases  $\phi$  with respect to the LO, namely,

$$\langle v | \hat{\varrho} | v' \rangle = \overline{\langle v | \hat{K}_\eta(x - \hat{X}_\phi) | v' \rangle}, \quad (33)$$

where the overbar denotes the experimental average. The functions  $\langle v | \hat{K}_\eta(x - \hat{X}_\phi) | v' \rangle$  for different vectors  $|v\rangle$  and  $|v'\rangle$  are called “pattern-functions” after Ref. [5].

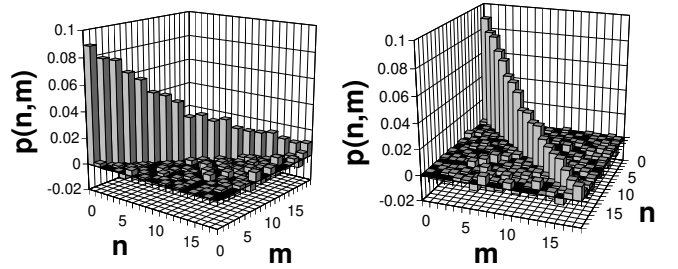


FIG. 3. Two-mode photon-number probability  $p(n, m)$  of the twin-beam state of parametric fluorescence in Eq. (15) (two different perspectives), obtained by a Monte-Carlo simulation of self-homodyne tomography at unit quantum efficiency for  $\bar{n} = 10$  and with  $10^6$  simulated data.

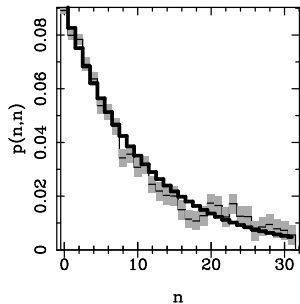


FIG. 4. Diagonal elements  $p(n, n)$  of Fig. 3 (shown by thin solid line on an extended abscissa range) with their respective error bars in gray shade, compared to the theoretical probability (17) (thick solid line).

In Ref. [4] the boundness of different types of matrix elements of the operator kernel  $\hat{K}_\eta(x - \hat{X}_\phi)$  was analyzed as a function of the quantum efficiency. It was shown that for the photon-number and coherent-state representations these matrix elements become unbounded for  $\eta \leq 1/2$ . The fact that  $\eta = 1/2$  is a lower bound for measuring the state in any (not exotic) representation was thoroughly discussed in Ref. [7]. The way in which nonunit quantum efficiency manifests its detrimental effect when approaching the lower bound is through increasingly large statistical errors. Let us restrict our attention to the photon-number representation. At  $\eta = 1$ , as proven in Ref. [25], the statistical errors of the diagonal matrix elements  $\langle n | \hat{\varrho} | n \rangle$  saturate at the limiting value  $\sqrt{2/N}$  for sufficiently large  $n$ , independently of the state  $\hat{\varrho}$  ( $N$  is the number of data collected in the experiment). Also, errors of the off-diagonal elements increase very slowly versus the distance from the main diagonal. On the other hand, for  $\eta < 1$  the errors increase dramatically versus either  $n$  or  $1 - \eta$ , and eventually become infinite at the lower bound  $\eta = 1/2$  [26]. In the next section we will see how this behavior manifests itself in the two-mode tomography measurement, on the basis of numerical results from Monte-Carlo simulation experiments.

## B. Multimode detection

It is easy to see that Eq. (27) can be extended because of linearity to the case of  $M$  modes as follows:

$$\hat{R} = \int_{\mathbf{C}^M} \prod_{l=1}^M \frac{d^2 w_l}{\pi} \text{Tr} \left[ \hat{R} \prod_{s=1}^M \hat{D}_s(w_s) \right] \prod_{r=1}^M \hat{D}_r^\dagger(w_r), \quad (34)$$

where  $\hat{R}$  now denotes the joint  $M$ -mode density operator, and  $\hat{D}_l(w_l)$  is the displacement operator for the  $l$ -th mode. As a consequence, Eq. (33) is extended to the multimode measurement in the following way:

$$\overline{\langle \Phi | \hat{R} | \Phi' \rangle} = \langle \Phi | \prod_{l=1}^M \hat{K}_{\eta_l}(x_l - \hat{X}_{\phi_l}^{(l)}) | \Phi' \rangle, \quad (35)$$

where  $|\Phi\rangle$  and  $|\Phi'\rangle$  are now multimode vectors, and the experimental average is taken over the random outcomes  $x_l$  of the joint homodyne measurement of quadratures  $\hat{X}_{\phi_l}^{(l)}$ ,  $l = 1, \dots, M$ , of all  $M$  modes with random LO phases  $\phi_l$  (we have also let the quantum efficiency to be different for each homodyne detector). Equation (35) agrees with the results obtained in Refs. [18].

## C. Two-mode tomography through self-homodyning

As we have seen in Section II, in the self-homodyne measurement one can jointly measure the quadratures  $\hat{X}_\phi^\uparrow$  and  $\hat{X}_\psi^\leftrightarrow$  of two different modes  $\hat{B}_\uparrow$  and  $\hat{B}_\leftrightarrow$ , and thus, in principle, perform a two-mode tomography of the OPA output. However, in order to perform two-mode tomography we need uncorrelated phases  $\phi$  and  $\psi$  for the quadratures, whereas in the self-homodyne measurement they are actually correlated. In fact, one has

$$\begin{aligned} \phi &= \arg(\alpha_\uparrow + \tau\alpha_\leftrightarrow^*), \\ \psi &= \arg(\alpha_\leftrightarrow + \tau\alpha_\uparrow^*). \end{aligned} \quad (36)$$

In the case when we are interested in the photon distribution of one mode only, we can assume  $\alpha_\leftrightarrow = 0$ . Then, by letting the phase of  $\alpha_\uparrow$  fluctuate with a uniform distribution from 0 to  $2\pi$ , one can perform one-mode tomography of Eq. (33). On the other hand, if we are interested in the joint photon-number distribution, then we can not make the measurement by simply averaging the two-mode pattern functions over the experimental outcomes as in Eq. (35). This is because the LO phases  $\phi$  and  $\psi$  in this case are not independent random variables. We will show, however, that it is possible to take the correlation of  $\phi$  and  $\psi$  into account and still perform two-mode tomography by appropriately weighting the experimental outcomes in Eq. (35). We first rewrite Eq. (35) in the two-mode case as follows:

$$\begin{aligned} \langle \Phi | \hat{R} | \Phi' \rangle &= \int_0^{2\pi} \frac{d\phi}{2\pi} \int_0^{2\pi} \frac{d\psi}{2\pi} \int_{-\infty}^{+\infty} dx \int_{-\infty}^{+\infty} dx' \\ &\times p(x, x'; \phi, \psi) \langle \Phi | \hat{K}_\eta(x - \hat{X}_\phi^\uparrow) \hat{K}_\eta(x' - \hat{X}_\psi^\leftrightarrow) | \Phi' \rangle. \end{aligned} \quad (37)$$

We focus our attention on the phase average only. For LO's with equal intensities  $|\alpha_\leftrightarrow| = |\alpha_\uparrow|$  and phases  $\varphi_\uparrow = \arg(\alpha_\uparrow)$  and  $\varphi_\leftrightarrow = \arg(\alpha_\leftrightarrow)$ , one has

$$\begin{aligned} \phi - \psi &= \varphi_\uparrow - \varphi_\leftrightarrow, \\ \phi + \psi &= \varphi_\uparrow + \varphi_\leftrightarrow + 2 \arg \left[ 1 + \tau e^{-i(\varphi_\uparrow + \varphi_\leftrightarrow)} \right]. \end{aligned} \quad (38)$$

After performing the change of variables

$$\begin{aligned} \sigma &= \frac{1}{2}(\varphi_\uparrow + \varphi_\leftrightarrow), \\ \delta &= \frac{1}{2}(\varphi_\uparrow - \varphi_\leftrightarrow), \end{aligned} \quad (39)$$

the average over the phases can be rewritten in terms of the average over the sum and difference phases with an appropriate weighting function as follows:

$$\int_0^{2\pi} \frac{d\phi}{2\pi} \int_0^{2\pi} \frac{d\psi}{2\pi} = \int_{-\pi}^{+\pi} \frac{d\delta}{2\pi} \int_0^{2\pi} d\sigma w(\sigma), \quad (40)$$

where the weighting function is given by

$$w(\sigma) = \frac{1}{2\pi} \frac{1 - \tau^2}{1 + \tau^2 + 2\tau \cos \sigma}. \quad (41)$$

Since the input phases  $\varphi_\uparrow$  and  $\varphi_\leftrightarrow$  can certainly be considered as random and uncorrelated, the same must hold true for their half-sum  $\sigma$  and half-difference  $\delta$  in Eq. (39). Then, the measurement of the matrix element in Eq. (37) is obtained by averaging over the experimental random phases  $\sigma$  and  $\delta$  with the weighting function (41). Also, the weighting function can be rewritten in terms of the gain  $g(\sigma)$  of the central-frequency component that is given by

$$g(\sigma) = \frac{|\mu\alpha_\uparrow + \nu\alpha_\leftrightarrow^*|^2}{|\alpha_\uparrow|^2} = \mu^2(1 + \tau^2 + 2\tau \cos \sigma). \quad (42)$$

Hence, the weighting function is simply

$$w(\sigma) = \frac{1}{2\pi g(\sigma)}, \quad (43)$$

which can be easily and independently measured for every data point while the homodyne data are collected.

This approach to phase averaging can also be used for detection of the  $\pm 45^\circ$  modes mentioned in Subsection II B. In that case, the quadrature phases  $\arg(\alpha_\nearrow + \tau\alpha_\nearrow^*)$  and  $\arg(\alpha_\nwarrow + \tau\alpha_\nwarrow^*)$  are independent, but non-uniformly distributed. Then, the averaging is done over the input phase  $\sigma = \arg(\alpha_\nearrow)$  or  $\sigma = \arg(\alpha_\nwarrow)$ , respectively, with the weighting function (43) given by the phase-sensitive gain of the central component.

#### D. Measuring the “bare” or the “dressed” state

For non-unit quantum efficiency one can measure the density matrix elements for  $\eta$  above the bound  $\eta = 1/2$ . However, instead of measuring the density matrix of the state  $\hat{R}$  of interest, one can always measure the density matrix of the state that has been damped—or “dressed”—by the quantum efficiency, without any limitation for  $\eta$ , even though such a dressed state would be less and less significant for lower quantum efficiencies. The concepts of “dressed” and “bare” states are two faces of the same measurement description when regarded in the equivalent Schrödinger and Heisenberg pictures. The conventional description corresponds to the Heisenberg picture, in which the true state—also called the “signal” or the “bare” state—is measured and the effect of quantum efficiency is ascribed to the detector observable (photocurrent). In the “dressed” state description, on the other hand, one regards the measurement with  $\eta < 1$  on the true state  $\hat{R}$  as the corresponding hypothetical “bare measurement” with  $\eta = 1$ , but now on the “dressed” state  $\hat{R}_\eta$ , ascribing the effect of the non-unit quantum efficiency to the quantum state itself, rather than to the detector. In other words, the effect of the non-unit quantum efficiency is regarded in a Schrödinger-like picture, with the state evolving from  $\hat{R}$  to  $\hat{R}_\eta$ , where the quantum efficiency plays the role of a time parameter.

An easy way to perform tomographic measurement on a dressed state is just to use the experimental data for  $\eta < 1$  and analyze them using the pattern function with  $\eta = 1$ . As shown in Subsection II B, the effect of non-unit quantum efficiency is to convolve the quadrature-probability distributions for all LO phases with a Gaussian of variance  $\Delta_\eta^2$  given by Eq. (13). This corresponds to convolving the Wigner function with an isotropic Gaussian of the same variance  $\Delta_\eta^2$  in the complex plane, which, in turn, corresponds to adding Gaussian noise to the quantum state. In terms of the bare state  $\hat{\varrho}$ , the state  $\hat{R}_\eta(\hat{\varrho})$  dressed with the Gaussian noise is given by [27]

$$\hat{R}_\eta(\hat{\varrho}) = \int \frac{d^2 w}{\pi \bar{n}} \exp(-|w|^2/\bar{m}) \hat{D}(w) \hat{\varrho} \hat{D}^\dagger(w), \quad (44)$$

where the noise-equivalent mean thermal photon number  $\bar{m}$  is related to the quantum efficiency through

$$\bar{m} = 2\Delta_\eta^2 = \frac{1-\eta}{2\eta}. \quad (45)$$

In the multimode case, one needs to apply the transformation (44) repeatedly, once per each mode, with the corresponding displacement operator of the mode. In the context of measuring the bare state, Eq. (44) was exploited in Ref. [28] to show that the measurement is possible even in the presence of quantum noise, however, with no more than  $\bar{m} = 1/2$  thermal photons.

Another way of dressing the state, which is often employed in experimental analysis of the tomographic data

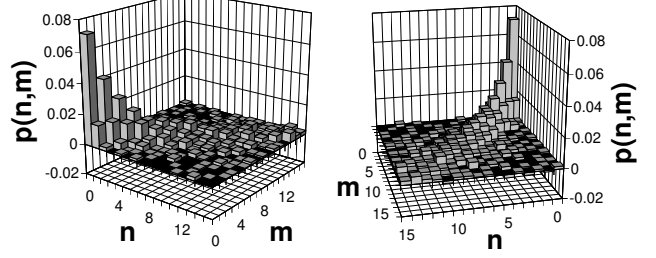


FIG. 5. Monte-Carlo simulation of self-homodyne tomography of the two-mode photon-number probability  $p(n, m)$  for quantum efficiency  $\eta = 0.8$  (two different perspectives). The state is the same as in Fig. 3, but in its Gaussian-noise dressed form  $\hat{R}_\eta(\hat{R})$  [see Eq. (44)]. Notice the smearing effect of the non-unit quantum efficiency.

(see Refs. [10,11,23]) is to consider the state that has undergone a loss equivalent to  $\eta$ . In this case, the analysis is done by rescaling the output photocurrents by  $\sqrt{\eta}$  instead of  $\eta$  as in Eqs. (4), and then using the pattern functions for  $\eta = 1$ . It is easy to see that this procedure corresponds to measuring the dressed state  $\hat{\Lambda}_\eta(\hat{\varrho})$ , which is related to the bare state  $\hat{\varrho}$  as follows:

$$\hat{\Lambda}_\eta(\hat{\varrho}) = \sum_{n=0}^{\infty} \frac{(\eta-1)^n}{n!} \hat{a}^n \eta^{-\frac{1}{2}\hat{a}^\dagger \hat{a}} \hat{\varrho} \eta^{-\frac{1}{2}\hat{a}^\dagger \hat{a}} (\hat{a}^\dagger)^n. \quad (46)$$

Again, in the multimode case the transformation (46) is applied separately to all modes. One can also regard the state  $\hat{\Lambda}_\eta(\hat{\varrho})$  in Eq. (46) as the state of the mode  $\sqrt{\eta} \hat{a} + \sqrt{1-\eta} \hat{v}$ —instead of the state of just the mode  $\hat{a}$  of interest—where  $\hat{v}$  is the independent vacuum-state mode responsible for the loss.

Before concluding this section, we need to say a few words regarding the difference between the two dressed states  $\hat{\Lambda}_\eta(\hat{\varrho})$  and  $\hat{R}_\eta(\hat{\varrho})$ . In the loss model corresponding to  $\hat{\Lambda}_\eta(\hat{\varrho})$ , the dressed state loses some signal, and becomes the vacuum state in the limit of  $\eta \rightarrow 0$ , independently of  $\hat{\varrho}$ , which makes the state less and less meaningful for decreasing  $\eta$ . On the other hand, in the Gaussian-noise model corresponding to  $\hat{R}_\eta(\hat{\varrho})$ , there is no loss of signal, but the state gets an increasingly large number of thermal photons for decreasing  $\eta$ . In this way, the most interesting quantum features of the state—as, for example, oscillations in the photon-number probability—are lost, as shown in Ref. [4], and all states tend to look “classical”. In the next section we will see these effects at work in some Monte-Carlo numerical experiments for the two-mode case.

#### IV. MONTE-CARLO SIMULATIONS

In this section we present some numerical results from Monte-Carlo simulations of the self-homodyne measure-

ment. Our aim is to analyze the feasibility of a real experiment and to see how many measurements are needed for a state reconstruction, especially in presence of the detrimental effect of non-unit quantum efficiency of the photodetectors. We will restrict our analysis to the measurement of the joint density matrix  $\hat{R}$  of the two modes,  $\hat{B}_\downarrow$  and  $\hat{B}_\leftrightarrow$ , assumed to be in the correlated state given by Eq. (15).

The simulation of the homodyne outcomes is based on the probability distribution in Eq. (21), which shows how the outcomes can be obtained from a Gaussian random generator, starting from the generation of  $x'$ , then generating  $x$ , and finally shifting the latter by  $c_\kappa x'$ . The phases  $\phi$  and  $\psi$  of the quadrature are chosen randomly for every sample. The density matrix in the photon-number representation is measured by averaging the pattern functions over the random data:

$$\langle n_1, m_1 | \hat{R} | n_2, m_2 \rangle = \overline{\langle n_1 | \hat{K}_\eta(x - \hat{X}_\phi) | n_2 \rangle \langle m_1 | \hat{K}_\eta(x' - \hat{X}_\psi) | m_2 \rangle}. \quad (47)$$

The pattern functions for a generic  $\eta$  are obtained from the pattern functions for  $\eta = 1$ , using the inverse generalized Bernoulli transformation as in Ref. [29]. The pattern functions for  $\eta = 1$ , in turn, are obtained from the factorization formulas of Refs. [8] (following our conventions for the quadratures, we actually use the factorization formulas as given in Ref. [7]). In Fig. 3 we show the results of a simulation for the measurement of the two-mode photon-number probability  $p(n, m)$  for unit quantum efficiency. The theoretically expected distribution, given by Eq. (17), is shown in Fig. 2(left). In Fig. 4 the diagonal elements  $p(n, n)$  of Fig. 3 are shown with their respective error bars, and compared against the theoretical probability of Eq. (17). From both Figs. 3 and 4 we see that there is an excellent agreement between the theoretically-obtained and tomographically-reconstructed joint probabilities, and the fluctuations in the latter are already very small for a number of data samples as low as  $10^6$ , which can be easily acquired within the stability time of a typical twin-beam setup.

In Figs. 5 and 6 the same tomographic measurement of Figs. 3 and 4 is reported, but now for a quantum efficiency  $\eta = 0.8$  for each detector. However, in the reconstruction, the pattern functions for  $\eta = 1$  are used. As explained in Subsection III D, this corresponds to a measurement of the state  $\hat{\Gamma}_\eta(\hat{R})$  that has been dressed by the Gaussian-noise equivalent of the quantum efficiency, instead of a measurement of the true twin-beam state. (For values of the quantum efficiency  $\eta = 0.8$  and  $\eta = 0.9$  used throughout this paper, the two kinds of state dressing—Gaussian-noise or loss—give similar qualitative results.) The smearing effect of the non-unit quantum efficiency is evident in Fig. 5, where the perfect photon-number correlation between the two modes is smudged, resulting in non-vanishing probabilities  $p(n, m)$  for  $n \neq m$ . Because of the preservation of the normalization in the  $(n, m)$

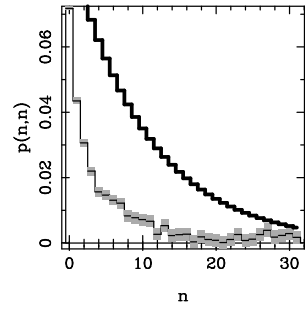


FIG. 6. The same as in Fig. 5, but for the diagonal elements  $p(n, n)$  only (thin solid line with error bars in gray shade), compared to the theoretical probability (17) for the bare state (thick solid line). The disagreement between the theoretical probability for the bare state  $\hat{R}$  and the simulated measurement for the dressed state  $\hat{\Gamma}_\eta(\hat{R})$  is a typical manifestation of the non-unit quantum efficiency.

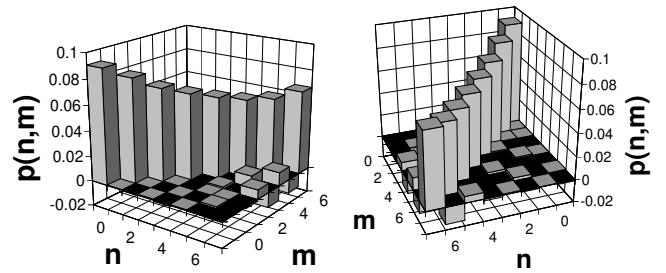


FIG. 7. Reconstruction of the bare state using the pattern functions with the correct experimental value of the quantum efficiency  $\eta$  (two different perspectives are shown). Here  $\bar{n} = 10$ ,  $\eta = 0.9$ , and we used  $10^7$  data samples for the Monte-Carlo simulation.

plane, the diagonal  $p(n, n)$  is decreased, resulting in the evident disagreement in Fig. 6, where the reconstructed diagonal elements  $p(n, n)$  are reported with relative error bars and compared with the theoretical probability (17) for the bare state.

In Fig. 7 we present the results of Monte-Carlo simulation for a realistic measurement of the bare state, but now using the pattern functions with the correct experimental value of the quantum efficiency  $\eta$ . One can see that the smearing effect of the non-unit quantum efficiency has been cleaned out, which, however, comes at the expense of increasing fluctuations for large  $n$ . This is even more evident in Fig. 8, where the reconstruction of the diagonal probability  $p(n, n)$  for the bare state is shown for two different values,  $\eta = 0.9$  and  $\eta = 0.8$ , of the quantum efficiency. One can see that there is no longer the disagreement between the reconstructed and the theoretical values, of the kind shown in Fig. 6, but now the error bars have increased dramatically for larger  $n$ , becoming worse for smaller  $\eta$  [cf. Fig. 8(right)].

The off-diagonal number probabilities and the correla-

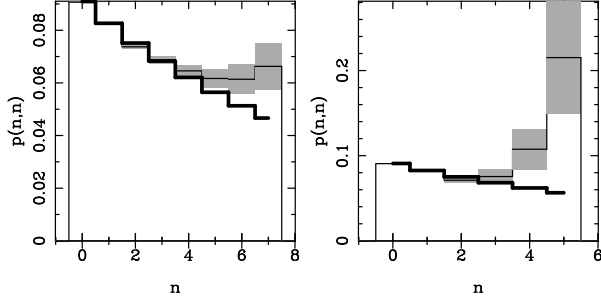


FIG. 8. Reconstruction of the diagonal probability  $p(n, n)$  for the bare state, using the pattern functions with the correct experimental value of the quantum efficiency  $\eta$ . Here  $\bar{n} = 10$  and  $\eta = 0.9(0.8)$  in the left (right) figure. The theoretical probability (thick solid lines) is superimposed onto the results of the Monte-Carlo experiments ( $10^7$  data samples); the latter are shown with thin solid lines with statistical errors in gray shade. Notice that there is no longer the disagreement shown in Fig. 6, but now error bars increase dramatically versus  $n$  and for smaller  $\eta$ .

tion between the two modes can be analyzed by evaluating the following sums of matrix elements:

$$s(n) = \sum_{l=0}^n \langle l, n-l | \hat{R} | l, n-l \rangle, \quad (48)$$

$$d_N(n) = \sum_{l=\max(-n,0)}^N \langle l, n+l | \hat{R} | l, n+l \rangle. \quad (49)$$

The quantity  $s(n)$  is the probability distribution for the total number of photons in the two modes. The theoretical result for our state in (15) is the oscillating function

$$s(n) = \begin{cases} (1 - \tau^2) \tau^{2n} & n \text{ even}, \\ 0 & n \text{ odd}, \end{cases} \quad (50)$$

similar to the photon-number distribution of a single-mode squeezed vacuum [11,17]. On the other hand, the quantity  $d_N(n)$  represents the photon-number correlation between the two modes, and in the limit  $N \rightarrow \infty$  is the Kronecker  $\delta_{n0}$  for a twin-beam state. For finite  $N$  its theoretical value for the state in Eq. (15) can be evaluated to be

$$d_N(n) = \delta_{n0}(1 - \tau^{2(N+1)}). \quad (51)$$

In Fig. 9 we show the results of a simulation of the total photon-number probability  $s(n)$ , Eq. (48), for  $\eta = 1$  and compare them to the theoretical value, Eq. (50). As shown, the theoretically-expected distribution is well reproduced from  $10^6$  data samples with very small statistical errors. In Fig. 10 a similar simulation is presented as in Fig. 9, but now for a quantum efficiency of  $\eta = 0.8$ . The total photon-number probability  $s(n)$  is reconstructed for both the dressed state and the bare

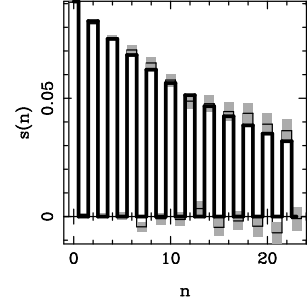


FIG. 9. Oscillations of the total photon-number probability  $s(n)$  in Eq. (48) due to the perfect correlation of the photon number in the twin-beam state, Eq. (15). Thin solid line with error bars in gray shade represents the results of a Monte-Carlo simulation with unit quantum efficiency,  $\bar{n} = 10$ , and  $10^6$  data samples. Thick solid line is the theoretical result, Eq. (50).

state. Once again, one can see the smearing effect of the quantum efficiency in the dressed-state case, where the oscillations of the total photon number are almost completely washed out. On the other hand, the oscillations are nicely recovered in the reconstruction of the bare state, albeit at the expense of increasingly large statistical errors. In Fig. 11 we present a simulation for  $\eta = 0.9$  to show how these quantum oscillations would be detected in an experimentally-feasible measurement of the dressed state with  $\bar{n} = 4$  and  $10^6$  data samples.

Regarding measurement of the photon-number correlation  $d_N(n)$  [Eqs. (49) and (51)], comments similar to those made for the total photon-number probability  $s(n)$  hold. Figure 12 presents the results of a simulation of the correlation function for the twin-beam state with  $N = \bar{n} = 10$  and unit quantum efficiency, whereas Fig. 13 shows the results of simulations with quantum efficiency  $\eta = 0.8$ , once again, reconstructing the correlation for both the dressed-state and the bare-state cases. Here also, the non-unit quantum efficiency in the case of dressed-state reconstruction partially smears out the correlation, which is well recovered in the case of bare-state reconstruction. In Fig. 14, we compare the reconstructed correlation function for the dressed state in Fig. 13(left) to that for two modes in uncorrelated coherent states, each having the same mean photon number  $\bar{n} = 10$  as the modes of the twin-beam state. One can see that, in spite of the detrimental effect of the non-unit quantum efficiency, the correlation for the reconstructed dressed state is still stronger than that for the uncorrelated coherent states, the latter representing the standard quantum limit.

## V. DISCUSSION

We have proposed a method for performing two-mode optical-homodyne tomography of the twin beams pro-

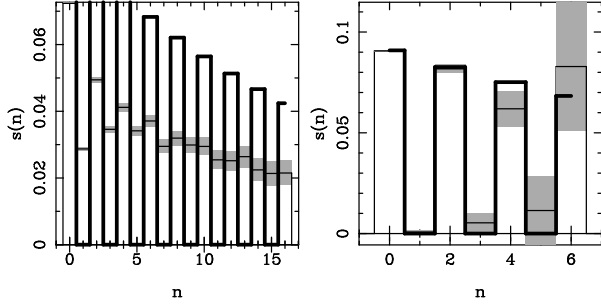


FIG. 10. Similar to Fig. 9, but for a quantum efficiency  $\eta = 0.8$ . Results for the Gaussian-noise-dressed state reconstruction are shown on the left and for the bare state reconstruction on the right. Here  $\bar{n} = 10$ , and we used  $5 \times 10^6$  data samples for the left plot and  $10^7$  data samples for the right plot. In the left plot, the ordinate is truncated at the maximum value of the simulated probability. The oscillations are nicely recovered in the right plot, wherein pattern functions with the correct value of quantum efficiency (0.8) were used for reconstruction..

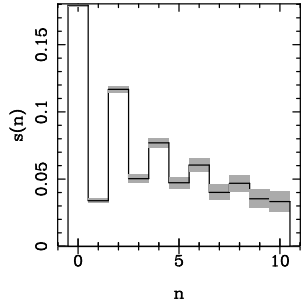


FIG. 11. Similar to Fig. 10(left), but for  $\eta = 0.9$ ,  $\bar{n} = 4$ , and  $10^6$  data samples.

duced from a nondegenerate optical parametric amplifier. The local oscillators (LO's) needed for the homodyne tomography are generated in the same parametric process as the twin beams, and, therefore, are automatically matched to the signal and idler twin-beam modes. In our self-homodyning method, the polarized central spectral component at  $\omega_0$  serves as the LO for a mode that consists of two sidebands at  $\omega_0 \pm \Omega$ , and the relative optical phase between the central component and the sidebands can be varied. We have presented a theoretical description for both one- and two-mode tomography, with main focus on measurement of the photon-number distributions. For the signal mode alone, a thermal distribution of photons is found, in agreement with the results of a recent experiment [23]. In the case of two modes, we have presented some selected Monte-Carlo simulations of the tomographic measurement of the joint photon-number distributions, choosing realistic values for the quantum efficiency of the photodetectors. In particular, we have analyzed the feasibility of detecting photon-number oscillations and delta-like photon correlation between the

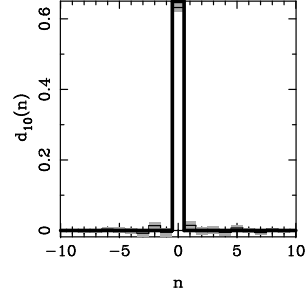


FIG. 12. Correlation function, Eq. (49), for the twin beam state in Eq. (15) with  $\bar{n} = 10$  and  $\eta = 1$  reconstructed from  $3 \times 10^5$  data samples. Results of the Monte-Carlo simulation (thin solid line with error bars in gray shade) are superimposed onto the theoretical correlation, Eq. (51), shown by thick solid line.

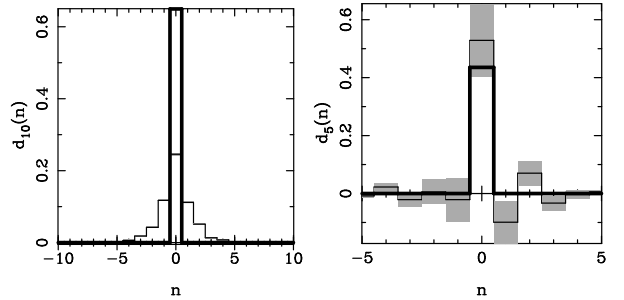


FIG. 13. Similar to Fig. 12, but for  $\eta = 0.8$ . Results for the Gaussian-noise-dressed state reconstruction are shown on the left and for the bare state reconstruction on the right. In both simulations  $5 \times 10^6$  data samples were used. The non-unit quantum efficiency in the dressed-state case partially smears out the correlation, which is recovered in the bare-state reconstruction (right), however at the expense of increasingly-large statistical errors.

twin-beam modes. We have shown that for ideal photodetectors such features can be clearly observed even with a small number of data samples ( $10^6$ ). However, for realistic quantum efficiencies the oscillations are exhibited with less contrast in the dressed-state reconstruction for the same number of data samples. On the other hand, for a tomographic measurement of the true output state of the OPA, more data samples are needed in order to reduce the statistical errors. Our Monte-Carlo simulations show that for a quantum efficiency of  $\eta = 0.9$ , the oscillations in the total photon number can be observed, even in the dressed-state reconstruction, with as little as  $10^6$  data samples, which makes such an experiment feasible.

We have also shown how the self-homodyning method can be used in detection of the  $\pm 45^\circ$ -polarized modes, instead of the signal and idler modes. Since in a polarization-nondegenerate optical parametric amplifier these modes are amplified independently, their joint photon-number distribution is factorized into a product

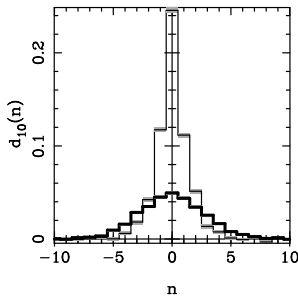


FIG. 14. Comparison of the correlation function, Eq. (49), for the Gaussian-noise-dressed state of Fig. 13(left), shown by thin solid line with error bars in gray shade, with that for two modes in uncorrelated coherent states (thick solid line), having the same mean photon number  $\bar{n} = 10$  per mode.

of marginal distributions, each exhibiting even-odd oscillations in its photon number.

While the focus of our paper has been on the twin-beam state, the self-homodyning approach can be applied in other instances as well. There are a number of mode-matching critical situations where it is possible to mix the signal with another mode that underwent a similar generation process. A key requirement in such situations would be the scanning of the relative phase between the two modes. Among potential applications are detection of the superposition (Schrödinger's cat) states, and squeezed states generated in optical fibers.

## APPENDIX

In this appendix we derive the joint probability distribution, Eq. (20), of the output photocurrents for two-mode homodyne detection.

In the Fock representation, the state at the output of the NOPA is given by Eq. (15), namely,

$$|\Psi\rangle = (1 - \tau^2)^{1/2} \sum_{n=0}^{\infty} \tau^n |n, n\rangle. \quad (52)$$

Expanding the Fock state  $|n\rangle$  in terms of the quadrature representation  $|x\rangle_{\phi}$  for each mode, one has

$$|\Psi\rangle = \sqrt{\frac{2(1 - \tau^2)}{\pi}} \int_{-\infty}^{+\infty} dx \int_{-\infty}^{+\infty} dx' e^{-x^2 - x'^2} \times \sum_{n=0}^{\infty} \frac{[\tau e^{-i(\phi+\psi)}]^n}{2^n n!} H_n(\sqrt{2}x) H_n(\sqrt{2}x') |x\rangle_{\phi} \otimes |x'\rangle_{\psi}, \quad (53)$$

where  $H_n(x)$  denotes the Hermite polynomial of degree  $n$ . Using the following identity [30], which is valid for any complex number  $z$ ,

$$\sum_{n=0}^{\infty} \frac{(\frac{1}{2}z)^n}{n!} H_n(x) H_n(x')$$

$$= (1 - z^2)^{-1/2} \exp \left\{ \frac{2xz - (x^2 + x'^2)z^2}{1 - z^2} \right\}, \quad (54)$$

we can rewrite Eq. (53) as

$$|\Psi\rangle = \left[ \frac{1 - |\kappa|^2}{1 - \kappa^2} \right]^{1/2} \sqrt{\frac{2}{\pi}} \int_{-\infty}^{+\infty} dx \int_{-\infty}^{+\infty} dx' |x\rangle_{\phi} \otimes |x'\rangle_{\psi} \times \exp \left[ \frac{4xz' \kappa - (x^2 + x'^2)(1 + \kappa^2)}{1 - \kappa^2} \right], \quad (55)$$

where  $\kappa = \tau \exp[-i(\phi + \psi)]$  (the choice of the branch for the square root in the normalization of the state vector (55) gives only an overall phase factor that is irrelevant for probabilities). Equation (55) corresponds to the following joint probability:

$$p(x, x'; \phi, \psi) = \frac{2}{\pi |d_{\kappa} d_{-\kappa}|} \exp \left[ -\frac{(x + x')^2}{d_{\kappa}^2} - \frac{(x - x')^2}{d_{-\kappa}^2} \right], \quad (56)$$

where  $d_{\kappa}^2 \doteq |1 + \kappa|^2 / (1 - |\kappa|^2)$ . Non-unit quantum efficiency of the photodetectors is taken into account by evaluating the convolution of the ideal joint probability in Eq. (56) with Gaussians for each mode of variances given by Eq. (13). This immediately leads to Eq. (20).

---

\* Also: *Theoretical Quantum Optics Group*, INFM, Unità di Pavia, via Bassi 6, I 27100 Pavia, Italy.  
 1 K. Vogel and H. Risken, Phys. Rev. A **40**, 2847 (1989).  
 2 D. T. Smithey, M. Beck, M. G. Raymer, and A. Faridani, Phys. Rev. Lett. **70**, 1244 (1993); D. T. Smithey, M. Beck, J. Cooper, and M. G. Raymer, Phys. Rev. A **48**, 3159 (1993); G. Breitenbach, T. Muller, S. F. Pereira, J.-Ph. Poizat, S. Schiller, and J. Mlynek, J. Opt. Soc. Am. B **12**, 2304 (1995).  
 3 G. M. D'Ariano, C. Macchiavello and M. G. A. Paris, Phys. Rev. A **50**, 4298 (1994); G. M. D'Ariano, Quantum Semiclass. Opt. **7**, 693 (1995).  
 4 G. M. D'Ariano, U. Leonhardt and H. Paul, Phys. Rev. A **52**, R1801 (1995); H. Paul, U. Leonhardt, and G. M. D'Ariano, Acta Physica Slovaca **45**, 261 (1995).  
 5 U. Leonhardt, H. Paul and G. M. D'Ariano, Phys. Rev. A **52** 4899 (1995).  
 6 D. S. Krämer and U. Leonhardt, Phys. Rev. A **55**, 3275 (1997); J. Phys. A: Math. Gen. **30**, 4783 (1997).  
 7 G. M. D'Ariano, *Measuring Quantum States*, in *Quantum Optics and Spectroscopy of Solids*, ed. by T. Hakioglu and A. S. Shumovsky, (Kluwer Academic Publisher, Amsterdam 1997), pp. 175-202.  
 8 Th. Richter, Phys. Lett. A **221** 327 (1996); Phys. Rev. A **53** 1197 (1996).  
 9 U. Leonhardt, M. Munroe, T. Kiss, Th. Richter, and M. G. Raymer, Opt. Comm. **127**, 144 (1996).

<sup>10</sup> M. Munroe, D. Boggavarapu, M. E. Anderson, and M. G. Raymer, Phys. Rev. A **52**, R924 (1995).

<sup>11</sup> S. Schiller, G. Breitenbach, S. F. Pereira, T. Müller, and J. Mlynek, Phys. Rev. Lett. **77** 2933 (1996); G. Breitenbach, S. Schiller, and J. Mlynek, Nature **387**, 471 (1997).

<sup>12</sup> U. Janicke and M. Wilkens, J. Mod. Opt. **42**, 2183, (1995); S. Wallentowitz, W. Vogel, Phys. Rev. Lett. **75**, 2932 (1995); S. H. Kienle, M. Freiberger, W. P. Schleich, and M. G. Raymer, in *Experimental Metaphysics: Quantum Mechanical Studies for Abner Shimony*, ed. S. Cohen et al. (Kluwer, Lancaster 1997), p. 121.

<sup>13</sup> T. J. Dunn, I. A. Walmsley, and S. Mukamel, Phys. Rev. Lett. **74**, 884 (1995).

<sup>14</sup> C. Kurtsiefer, T. Pfau, and J. Mlynek, Nature **386**, 150 (1997).

<sup>15</sup> D. Leibfried, D. M. Meekhof, B. E. King, C. Monroe, W. M. Itano, and D. J. Wineland, Phys. Rev. Lett. **77**, 4281 (1996).

<sup>16</sup> H. Paul, P. Törmä, T. Kiss, and J. Jex, Phys. Rev. Lett. **76** 2464 (1996); O. Steuernagel and J. A. Vaccaro, Phys. Rev. Lett. **75** 3201 (1995); K. Banaszek and K. Wódkiewicz, Phys. Rev. Lett. **76** 4344 (1996); A. Zucchetti, W. Vogel, and D.-G. Welsch, Phys. Rev. A **54**, 856 (1996); M. Freiberger and A. M. Herkommer, Phys. Rev. Lett. **72** 1952 (1994); M. S. Zubairy, Phys. Lett. A **222**, 91 (1996); S. Wallentowitz and W. Vogel, Phys. Rev. A **53** (1996); S. Mancini, V. Man'ko, and P. Tombesi, Europhysics Lett. **37**, 79 (1997); P. J. Bardschaff, E. Mayr and W. P. Schleich, Phys. Rev. A **51**, 4963 (1995); L. G. Lutterbach and L. Davidovich, Phys. Rev. Lett. **78**, 2547 (1997); U. Leonhardt and M. G. Raymer, Phys. Rev. Lett. **76**, 1985 (1996); T. Opatrny, D.-G. Welsch, Phys. Rev. A **55**, 1462 (1997).

<sup>17</sup> R. S. Bondurant, B. S. thesis, MIT, 1978 (unpublished); W. Schleich and J. A. Wheeler, Nature **326**, 574 (1987); J. Huang, and P. Kumar, Phys. Rev. A **40**, 1670 (1989); P. Kumar, and J. Huang, *Quantum Optics V*, Springer Proceedings in Physics **41**, Ed. J. D. Harvey and D. F. Walls (Springer-Verlag Berlin, Heidelberg, 1989).

<sup>18</sup> H. Kühn, D.-G. Welsch, W. Vogel, Phys. Rev. A **51**, 4240 (1995); M. G. Raymer, D. F. McAlister, and U. Leonhardt, Phys. Rev. A **54**, 2397 (1996); T. Opatrny, D.-G. Welsch, W. Vogel, Opt. Comm. **134**, 112 (1997).

<sup>19</sup> T. Opatrny, D.-G. Welsch, W. Vogel, Phys. Rev. A **55**, 1416 (1997).

<sup>20</sup> D. F. McAlister, and M. G. Raymer, Phys. Rev. A **55**, R1609 (1997).

<sup>21</sup> J. H. Shapiro, A. Shakeel, J. Opt. Soc. Am. B **14**, 232 (1997); D. Levandovsky, PhD Proposal, Northwestern University, 1996 (unpublished).

<sup>22</sup> O. Aytur, P. Kumar, Opt. Lett. **17**, 529 (1992); C. Kim, P. Kumar, Phys. Rev. Lett. **73**, 1605 (1994).

<sup>23</sup> M. V. Vasilyev, M. L. Marable, S.-K. Choi, P. Kumar, and G. M. D'Ariano, *Self-homodyne tomography: Measurement of the photon statistics of parametric fluorescence*, in *Quantum Electronics and Laser Science Conference*, Vol. 12, 1997 OSA Technical Digest Series (Optical Society of America, Washington, D.C., 1997), pp. 95-96.

<sup>24</sup> G. M. D'Ariano, *Quantum Estimation Theory and Optimal Detection*, in the same book as Ref. [7], pp. 139-174.

<sup>25</sup> G. M. D'Ariano, C. Macchiavello, and N. A. Sterpi, Quantum Semiclass. Opt. **9** 929 (1997).

<sup>26</sup> G. M. D'Ariano and C. Macchiavello, (unpublished) (preprint: quant-ph/9701009).

<sup>27</sup> M. J. W. Hall, Phys. Rev. A **50** 3295 (1994).

<sup>28</sup> G. M. D'Ariano, in *Quantum Communication, Computing, and Measurement*, Edited by O. Hirota, A. S. Holevo, and C. M. Caves, Plenum Publishing (New York and London 1997), p. 253.

<sup>29</sup> T. Kiss, U. Herzog, and U. Leonhardt, Phys. Rev. A **52**, 2433 (1995).

<sup>30</sup> J. Bateman, *Higher transcendental functions*, McGraw-Hill (New York, Toronto, London 1953).